Experimental and numerical analyses of the mechanical behavior during draping of non-orthogonal bi-axial non-crimp fabric composite reinforcements

Eduardo Guzman-Maldonado, Sylvain Bel, Dominic Bloom, Paulin Fideu, Philippe Boisse

Experimental and numerical analyses of the mechanical behavior during draping of non-orthogonal bi-axial non-crimp fabric composite reinforcements

Guzman-Maldonado Eduardo[a], Bel Sylvain[b], Bloom Dominic[c], Fideu Paulin[d], Boisse Philippe[e]*

[a] Innovamics, 87 Av. des Frères Perret, Saint-Fons F-69190, France
[b] University of Lyon, LMC2, 82 Boulevard Niels Bohr, F-69622, France
[c] Expleo Engineering UK limited,1The Brooms, BS16 7FD Emersons Green, Bristol, UK
[d] Airbus Operations GmbH, Kreetslag 10, 21129 Hamburg, Germany
[e] University of Lyon, LaMCoS, CNRS, INSA Lyon, F-69621, France

Abstract

Experimental analyses and modeling of the draping of composite fiber reinforcements generally concern textiles where the fiber directions are orthogonal in the initial state. However, there also exist biaxial NCF (Non-Crimp Fabric) reinforcements, where the two fiber directions are non-orthogonal. One objective of this paper was to revisit the picture frame and bias extension tests in the case of such non-orthogonal NCFs in order to determine the in-plane shear behavior which is different for positive and negative shear angles. A simulation approach based on stress resultant shell elements was developed for these reinforcements by taking into account the specific plane shear behavior of non-orthogonal NCF reinforcements identified by picture frame tests. It was shown that simulations of non-orthogonal NCF (0-45° and 0/135°) draping processes gave results that were consistent with experimental forming tests of these materials. In particular, the hemispherical forming of an NCF at 0-45° led to a very specific deformed shape with a good correlation between simulation and experiment. Some specificities of the 0-45° preforms, especially weak areas, have been highlighted both by simulation and experimentally.

Key words: Non-Crimp Fabric; Non-orthogonal fibers, Picture Frame; Bias Extension Test; Draping;

1. Introduction

Continuous fiber composite materials make it possible to produce structures with high mechanical strength combined with low mass. Nevertheless, the manufacturing, particularly the shaping, of these materials is complex. To facilitate the development of such processes, simulation tools have been designed over the last

* Corresponding author : philippe.boisse@insa-lyon.fr

two decades. Methods and software have been developed in particular for the forming of textile preforms [1–11] and for the injection of the resin into the preform [12–17]. Among continuous fiber textile reinforcements, Non-Crimp Fabric (NCF) presents certain advantages. This material is composed of one or more layers of unidirectional reinforcements that are joined together by stitching. Composites reinforced with NCF have high mechanical properties and are widely used in the aerospace and automotive industries. The present work has involved biaxial NCF, i.e., composed of two layers of unidirectional (UD) reinforcements which is the most frequent case. The composition of the NCF reinforcements has the advantage that the fibers remain straight. The tension properties of the reinforcement are not diminished by the crimp present in the weave.

The use of NCF reinforcements with non-orthogonal yarn directions is being considered for certain aerospace and wind turbine components. The objective is to improve the design of these components with a new type of material. In order to use these non-orthogonal NCFs, simulation tools are needed, especially methods to simulate the draping of these materials which deform in a very particular way. This has been the perspective of the present work.

Studies of the mechanical behavior of NCF have been carried out. The Kawabata Evaluation System for Fabrics (KES-F) was used in [18] to determine the deformability of these reinforcements. Articles presenting the characterization of the inner structure of the material [19,20] and analyses of the behavior of the NCF-reinforced composite, in particular damage and fractures [21,22] or fatigue behavior [23], have been published. Concerning the mechanical behavior during draping, the deformation modes were studied in [24,18,25,26] and compared to those of woven fabrics. The in-plane shear behavior of the reinforcement was often asymmetrical, and depended on the position and orientation of the stitching. When draping on a symmetrical geometry, for instance a hemispherical shape, the obtained preform was asymmetrical [27]. Models of mechanical behavior during NCF forming have been developed in order to carry out draping simulations [27,28] and their objective was to express the asymmetry of the in-plane shear behavior. In [29,30], each biaxial NCF layer was modeled by shell elements and the two layers were linked by a bar with a constrained displacement with respect to the fibrous layers.

In all these studies and models concerning the properties of biaxial NCFs during forming, the two fiber layers were orthogonal in the initial position. This is the case of woven reinforcements where the weft and warp are perpendicular due to the weaving technology. In the case of biaxial NCF, the two fiber layers can be stitched in non-orthogonal initial positions, e.g., [0°, +45°] or [0°, -135°]. Such NCFs are used to bring different fiber directions into laminated composite parts and have a special place in aeronautical applications.

The equations used in the analysis of properties from classical experimental trials (picture frame test and bias extension test [31–35]) and numerical simulation models have been written for orthogonal directions for woven fabrics and orthogonal NCFs. The objective of this paper was thus to first revisit the picture frame and bias extension tests for biaxial NCF reinforcements in the case of any angle β between the two fiber directions. A simulation approach based on stress resultant shell elements was then developed for non-orthogonal NCFs. Finally, some draping simulations were carried out to show the good agreement with the

draping experiments, and also to highlight certain particularities about the deformation mechanisms of these materials that must be considered after the forming process.

2. In-plane shear characterization

The mechanical characterization of in-plane shear properties of orthogonal fabrics is a subject that has been widely discussed in the last few years [31-38], mainly because in-plane shear is the main deformation mode during forming. The deformation of a textile reinforcement involves a shear angle, which is defined by the following relationship:

$$\gamma(t) = \frac{\pi}{2} - \alpha(t) \tag{1}$$

where α is the angle between the warp and weft yarns at a given time t, and $\frac{\pi}{2}$ corresponds to the initial angle between these yarns. In the case of non-orthogonal NCF, the relationship can be generalized for an arbitrary initial angle β according to:

$$\gamma(t) = \beta - \alpha(t) \tag{2}$$

2.1. Shear angle convention

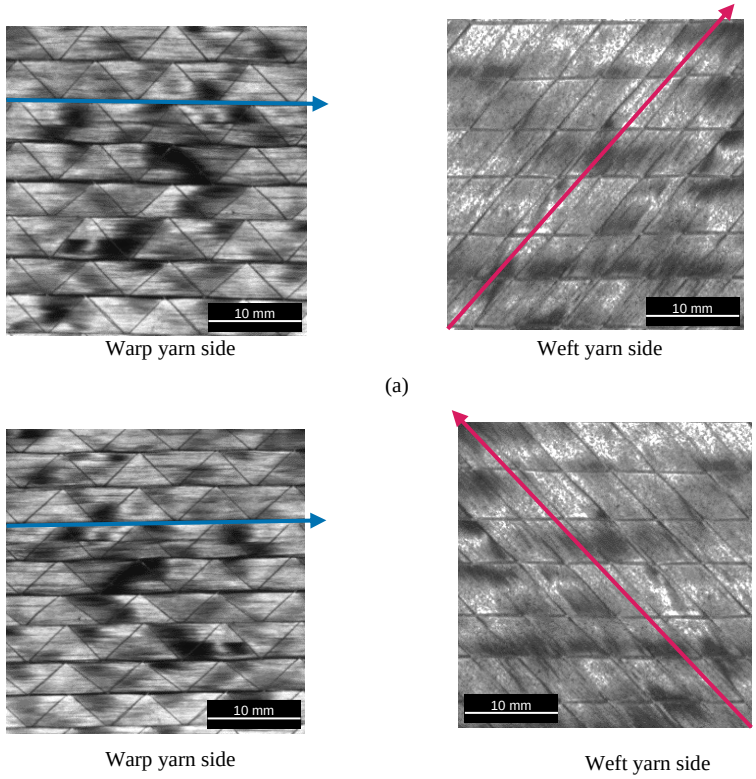

Figure 1 Non-orthogonal biaxial NCF reinforcement. (a) 0°/45° and (b) 0°/135° orientations.

Based on the above definition, it is possible to distinguish between negative and positive shearing. In the case of woven fabrics, this distinction is meaningless since the shear behavior is generally symmetrical. However, in the case of non-orthogonal NCF, the stitching process induces an asymmetrical behavior, wherefore it is important to consider both a positive and a negative in-plane shearing. This sign of the shear angle is a convention and depends on the initial angle between the warp and the weft yarns. The positive and negative shear angles are illustrated in Figure 2 for both 0°/45° and 0°/ 135° NCFs.

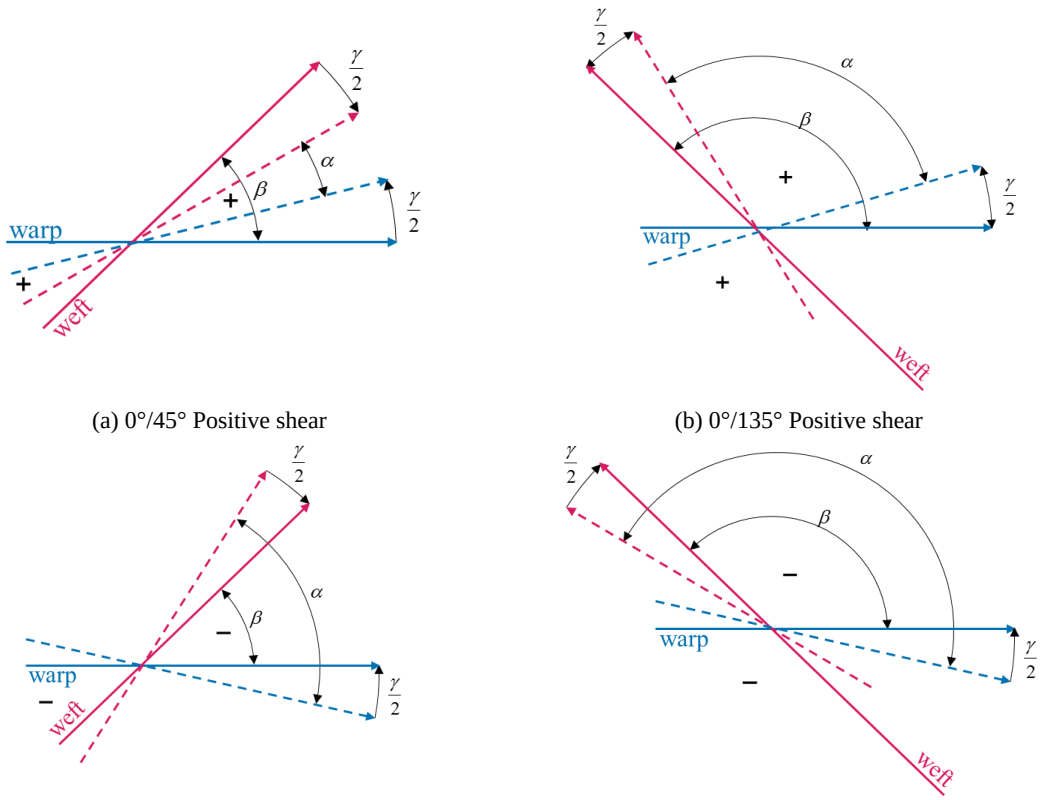

(a) 0°/45° Positive shear

(b) 0°/135° Positive shear

(c) 0°/45° Negative shear

(d) 0°/135° Negative shear

Figure 2 Definition of positive and negative shear angles for 0°/45° and 0°/135° configurations.

A proper definition of the sign of the in-plane shear angle is necessary not only to obtain an asymmetrical behavior but also to model the dissipative behavior of textiles during forming [39].

2.2. Picture Frame for non-orthogonal biaxial NCFs

The picture frame test is used to characterize the in-plane shear behavior of orthogonal woven fabrics. This test consists in placing a fabric on an articulated frame with the directions of the fibers parallel to the sides of the device (Figure 3a). The frame is positioned in a universal testing machine and loaded at two opposite points on the diagonal D. Theoretically, this type of stress provides pure shear kinematics on the entire specimen. The theoretical shear angle depends on the imposed displacement d and on the length L_c of the

frame side, according to the following relationship [35]:

$$\gamma(d) = \frac{\pi}{2} - 2\arccos\left(\frac{d+D}{2L_c}\right) \tag{4}$$

The shear moment M_{sh} per unit area and the normalized shear force F_{sh} are obtained from the pulling force F and the effective area of the specimen (L_m^2) according to:

$$M_{sh} = \frac{L_c}{L_m^2} F \sin\left(\frac{\alpha}{2}\right) \tag{5}$$

$$F_{sh} = \frac{M_{sh}}{\cos(\gamma)} = \frac{L_c}{L_m^2} \frac{F}{2\cos\left(\alpha\frac{\alpha}{2}\right)} \tag{6}$$

These equations are suitable for orthogonal materials and a square-shaped initial state of the picture frame. However, to characterize the behavior of a non-orthogonal fabric, the picture frame must be pre-sheared to align the sides of the device with the initial configuration of the material. The equations should be generalized to take into account the initial angle β (Figure 3b).

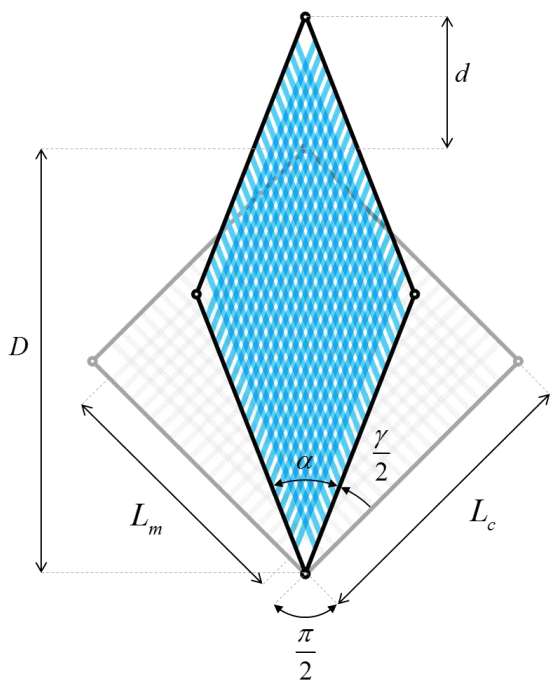

(a) Reinforcement with initially perpendicular yarns

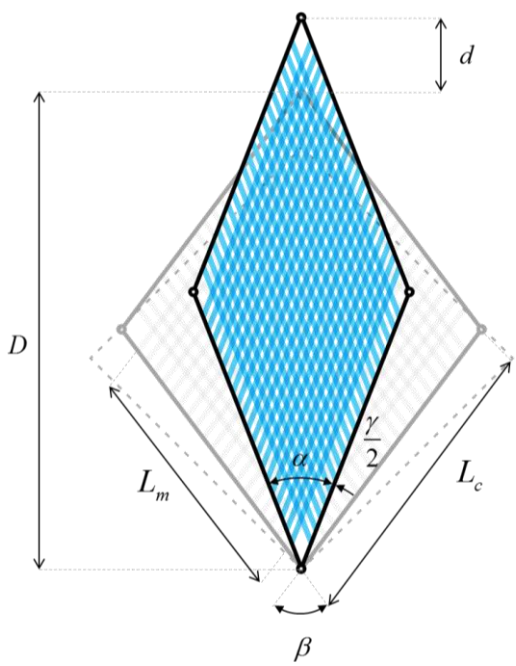

(b) Reinforcement with initially non-perpendicular yarns

Figure 3 Kinematics and parameterization of the picture frame test

This section considers only the mechanical energy, and the temperature is assumed to be constant. Under such conditions, the shear moment can be determined using the balance of mechanical energy. The external power due to the tensile load F can be related to the internal power due to the generalized in-plane shear moments:

$$F\dot{d} = \int_{S_A} M_{sh}(\gamma)\dot{\gamma}\,\mathrm{d}S \tag{7}$$

Here, S_A is the initial surface of the sample. After integration on the initial surfaces, we get:

$$F\dot{d} = M_{sh}(\gamma)\dot{\gamma}S_A \tag{8}$$

The time derivative of the shear angle is obtained by using a chain rule in Eq.(4).

$$\dot{\gamma} = -\frac{\partial\alpha}{\partial d}\dot{d} \tag{9}$$

$$\frac{\partial\alpha}{\partial d} = -\frac{1}{\sqrt{1-\left(\dfrac{D+d}{2L_c}\right)^2}}\frac{1}{L_c} = -\frac{1}{L_c\sin\left(\dfrac{\alpha}{2}\right)} \tag{10}$$

$$\dot{\gamma} = \frac{1}{L_c\sin\left(\dfrac{\alpha}{2}\right)}\dot{d} \tag{11}$$

Based on Eq.(8) and Eq.(11), the shear moment can be expressed as:

$$M_{sh} = \frac{FL_c}{S_A}\sin\left(\frac{\alpha}{2}\right) \tag{12}$$

Introducing the initial sheared area of the sample S_A:

$$S_A = L_m^2\sin(\beta) \tag{13}$$

Finally, using Eq.(12) and Eq.(13), the shear moment is given by:

$$M_{sh}(\gamma) = \frac{FL_c}{L_m^2}\frac{\sin\left(\dfrac{\beta-\gamma}{2}\right)}{\sin(\beta)} \tag{14}$$

The standard relation is recovered when $\beta = \frac{\pi}{2}$.

2.3. Bias extension test for non-orthogonal biaxial NCF

In the case of orthogonal materials, the bias-extension test comprises a tensile test on a rectangular textile reinforcement such that the directions of the warp and weft yarns are initially orientated at 45° to the direction

of the applied tension (Figure 4a). If there is no slip between the warp and weft yarns, and assuming that the yarns are inextensible, the deformation in zone Z_A is in pure shear. The shear angle in zone Z_B is half of that in zone Z_A, and zone Z_C remains undeformed (Figure 4b).

The shear moment M_{sh} per unit area and the normalized shear force F_{sh} are given by [36]:

$$M_{sh} = \frac{L_c}{S_A} F \sin\left(\frac{\alpha}{2}\right) - \frac{1}{2}\frac{S_B}{S_A} M_{sh}\left(\frac{\gamma}{2}\right) \tag{15}$$

$$F_{sh} = \frac{M_{sh}}{\cos(\gamma)} \tag{16}$$

where $S_A = L\,l - \frac{3}{2}l^2$ and $S_B = l^2$ are the initial surfaces of zone A and B, respectively.

The kinematics on which the bias extension test is based is the same regardless of the initial angle between the yarns. Therefore, the test can be used for the characterization of non-orthogonal fabrics. In order to adapt the equations for any configuration, a generalized configuration of the bias-extension test for an initial angle β between the yarns is considered (Figure 4b).

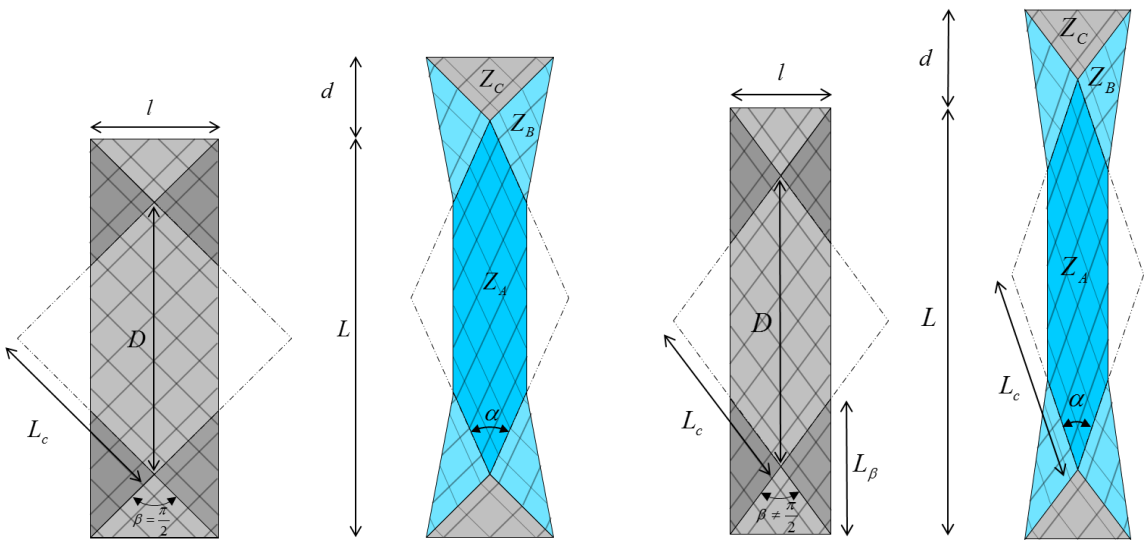

(a) Reinforcement with initially perpendicular yarns (b) Reinforcement with initially non-perpendicular yarns

Figure 4 Kinematics and parameterization of the Bias-extension test

It is useful to introduce the expression of the diagonal *D* in zone A as a function of the angle β.

$$D = L - L_\beta = L - \frac{l}{\tan\left(\frac{\beta}{2}\right)} \tag{17}$$

Here, L_β corresponds to the diagonal of the virtual frame in zone B and the length L_c of the virtual frame side is expressed as:

$$L_c = \frac{D}{2\cos\left(\frac{\beta}{2}\right)} \tag{18}$$

Alternatively, using the previous definition:

$$L_c = \frac{1}{2}\left(\frac{L}{\cos\left(\frac{\beta}{2}\right)} - \frac{l}{\sin\left(\frac{\beta}{2}\right)}\right) \tag{19}$$

The initial surfaces of zones A, B and C are given by:

$$S_C = \frac{S_B}{2} = \frac{l\,L_\beta}{2} = \frac{l^2}{2\tan\left(\frac{\beta}{2}\right)} \tag{20}$$

$$S_A = l\,L - S_B - S_C = l\,L - \frac{3}{2}\frac{l^2}{\tan\left(\frac{\beta}{2}\right)} \tag{21}$$

It is important to highlight that the trellis kinetics in zone A is only possible if $L \geq 2L_\beta$ (see Figure 4b), which defines the minimal ratio for the sample dimensions:

$$\frac{L}{l} \geq \frac{2}{\tan\left(\frac{\beta}{2}\right)} \tag{22}$$

As before, an energetic approach is used to determine the shear moment.

$$F\dot{d} = S_A M_{sh}(\gamma_A)\dot{\gamma}_A + S_B M_{sh}(\gamma_B)\dot{\gamma}_B \tag{23}$$

Since the trellis kinematics is respected, the shear angle in zone B is half of that in zone A. Consequently:

$$F\dot{d} = S_A M_{sh}(\gamma)\dot{\gamma} + \frac{1}{2}S_B M_{sh}\left(\frac{\gamma}{2}\right)\dot{\gamma} \tag{24}$$

Using Eq.(11), the external force is expressed as:

$$F = \frac{1}{L_c \sin\left(\frac{\alpha}{2}\right)}\left(M_{sh}(\gamma)\ S_A + \frac{1}{2}S_B M_{sh}\left(\frac{\gamma}{2}\right)\right) \tag{25}$$

And finally, the in-plane shear moment is given by:

$$M_{sh}(\gamma) = \frac{L_c}{S_A} F \sin\left(\frac{\beta-\gamma}{2}\right) - \frac{1}{2}\frac{S_B}{S_A} M_{sh}\left(\frac{\gamma}{2}\right) \quad (26)$$

It should be noted that this equation is equivalent to Eq.(15), but the geometrical constants L_c, S_B and S_A, obtained by expressions (19), (20) and (21), respectively, now take into account the initial angle β. The standard relation is recovered when $\beta = \frac{\pi}{2}$.

2.4. Characterization of the in-plane shear behavior of a non-orthogonal bi-axial non-crimp fabric

The negative and the positive shear behavior of a 0°/45° NCF material was characterized using the picture frame test. The tests were performed in a 100-mm picture frame device as shown in Figure 5. In order to test the positive shear behavior, the initial angle β was set to 45° (Figure 5a). A tensile load induced a positive shear

(a) Positive shear testing

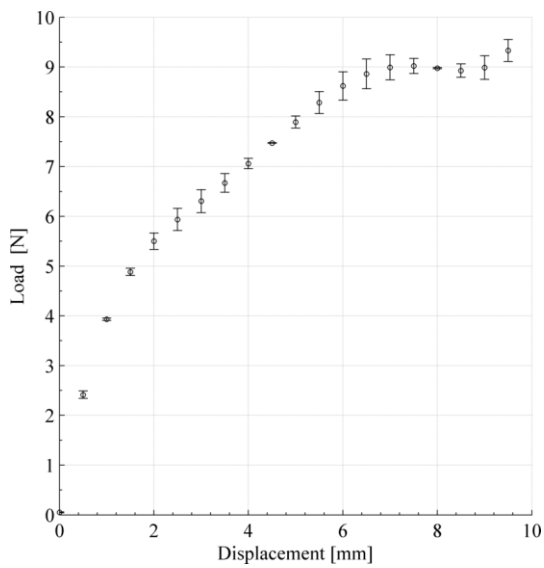

(a) Experimental force - positive shear

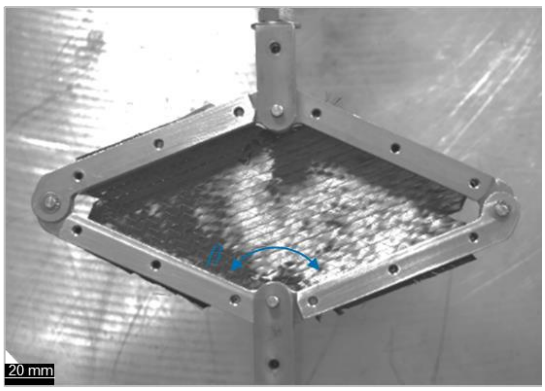

(b) Negative shear testing

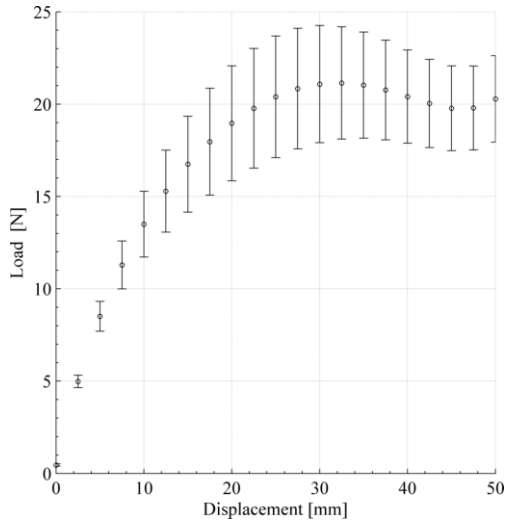

(b) Experimental force - negative shear

Figure 5 Experimental picture frame test on a 0°/45° NCF material.

field in the sample. However, since the frame was already sheared, only a small displacement of 10 mm could be applied, corresponding to a "positive" shear angle close to 12°. For the negative behavior, the initial angle β was set to 135° (Figure 5c), and this way, a tensile load induced a negative shear field. In contrast to the previous test, the displacement stroke was wide, making it possible to characterize the material for large "negative" shear angles (-45°)(Figure 5d). The tests were performed three times for each case using different samples. The shear moment curve was deduced from Eq.(15) and Figure 6a exhibits the highly asymmetrical response of the material. As a reference, the deduced shear moment which would be obtained using the equations for orthogonal materials was also plotted as a thin black line.

Figure 6b shows the asymmetric response of the non-orthogonal reinforcement, compared to the behavior of an orthogonal fabric (0°/90°).

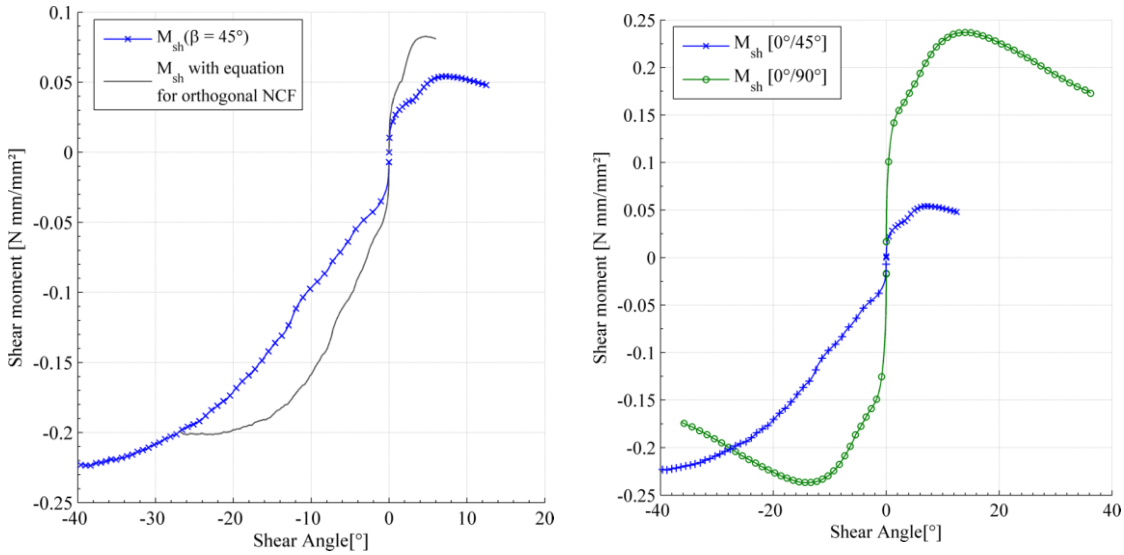

(a) (b)

Figure 6 NCF 0°/45° (a) Experimental shear moment taking into account an initial angle $\beta = 45°$ (this article) vs an initial angle of $\beta = 90°$ (orthogonal fabrics) (b) Comparison of the curve profile with an orthogonal symmetrical fabric (0°/90).

3. Draping modeling for non-orthogonal biaxial NCF

Several approaches have been proposed for the modeling and simulation of the forming processes for textile reinforcements and they can be categorized as either macroscopic (continuous) or mesoscopic (discrete) [40,41]. Discrete methods are well suited to the modeling of non-orthogonal materials since the yarns are modeled independently and the initial orientation is given explicitly. The global behavior of the material depends on the interactions between the different bodies and the constitutive behavior of the yarns [42–44]. However, it is difficult and often impossible to simulate the forming process of large parts due to the computational time being cost-prohibitive.

In the case of continuous materials, different models, such as hypoelastic [45–47] and hyperelastic [48–53] ones, are used. The hyperelastic models proposed in the literature are not adapted for the modeling of non-orthogonal materials. Indeed, the symmetry of the material at the initial state is a condition for the formulation of physical invariants. Hypoelastic models, on the other hand, constitute an interesting possibility; the strain and stress rates are calculated in an incremental way and independently from the initial state of the material. The main difficulty lies in establishing an objective basis for the calculation of strain and stress contributions [47,54]. Another option is to use a stress-resultant shell approach with elastic relations between the stress resultants and the membrane strains on the one hand and between the resultant couple and the curvatures on the other hand [55–57].

3.1. Stress-resultant shell approach

The model is based on the following form of the internal virtual work. For a fabric unit cell (Figure 7a), the

internal virtual work is the sum of the virtual work of tension W_{int}^{t}, the virtual work of in-plane shear W_{int}^{s}, and the virtual work of bending W_{int}^{b}:

$$W_{int}\left(\underline{\eta}\right) = W_{int}^{t}\left(\underline{\eta}\right) + W_{int}^{s}\left(\underline{\eta}\right) + W_{int}^{b}\left(\underline{\eta}\right) \tag{27}$$

where $\underline{\eta}$ is an arbitrary virtual displacement field. The different internal virtual works are related to stress resultants (Figure 7a):

$$W_{int}^{t}\left(\underline{\eta}\right) = \varepsilon_{11}\left(\underline{\eta}\right) T^{11} L_1 + \varepsilon_{22}\left(\underline{\eta}\right) T^{22} L_2 \tag{28}$$

$$W_{int}^{s}\left(\underline{\eta}\right) = \gamma\left(\underline{\eta}\right) M^{sh} \tag{29}$$

$$W_{int}^{b}\left(\underline{\eta}\right) = \chi_{11}\left(\underline{\eta}\right) M^{11} L_1 + \chi_{22}\left(\underline{\eta}\right) M^{22} L_2 \tag{30}$$

where T^{ii} are the tensile forces in the warp and weft directions that depend on the axial strains ε_{ii}, M^{sh} is the in-plane shear moment related to the in-plane shear angle and M^{ii} are the bending moments that depend on the curvatures.

The material coordinates $\left(r^1, r^2\right)$ are defined along the warp and weft yarns and designate the material vectors $\underline{k}_1, \underline{k}_2$ in the yarn directions that constitute a material basis. They are not necessarily initially perpendicular, thus making the method suitable for non-orthogonal fabrics.

The virtual axial strains in the warp and weft directions and the virtual shear angle are given as a function of the virtual displacement by:

$$\varepsilon_{ii}\left(\underline{\eta}\right) = \frac{\partial \underline{\eta}}{\partial r^i} \cdot \frac{\partial \underline{k}_i}{\underline{k}_i^{\,2}} \tag{31}$$

$$\gamma\left(\underline{\eta}\right) = \left(\underline{\underline{\nabla}}\underline{\eta} \cdot \frac{\underline{k}_1}{\left\|\underline{k}_1\right\|}\right) \cdot \frac{\underline{k}^2}{\left\|\underline{k}^2\right\|} + \left(\underline{\underline{\nabla}}\underline{\eta} \cdot \frac{\underline{k}_2}{\left\|\underline{k}_2\right\|}\right) \cdot \frac{\underline{k}^1}{\left\|\underline{k}^1\right\|} \tag{32}$$

The simulation is based on an explicit scheme [58,59] and is performed step by step. The strains are obtained by cumulation over the time steps:

$$\varepsilon_{ii}^{n+1} = \varepsilon_{ii}^{n} + \left\langle B_{ii} \right\rangle \left\{ \Delta u^{n+1} \right\} \quad , \quad \gamma^{n+1} = \gamma^{n} + \left\langle B_{\gamma} \right\rangle \left\{ \Delta u^{n+1} \right\} \tag{33}$$

Here, $\boldsymbol{B}_{ii}$ and $\boldsymbol{B}_{\gamma}$ are the tension and in-plane shear strain interpolation matrices and Δu^{n+1} are the nodal displacement increments at time t^{n+1}. Finally, the bending behavior is calculated using a rotation-free approach. The curvature in the warp and weft directions is related to the nodal displacement of the element and to those of the nodes of neighboring triangles [60-62] (Figure 7b). Details on the formulation of the finite

shell element in the case of woven reinforcements are given in [57]. The curvatures at time t^{n+1} are obtained by:

$$\chi_{ii}^{\,n+1} = \chi_{ii}^{\,n} + \langle B_{ii} \rangle \{ \Delta u^{n+1} \} \tag{34}$$

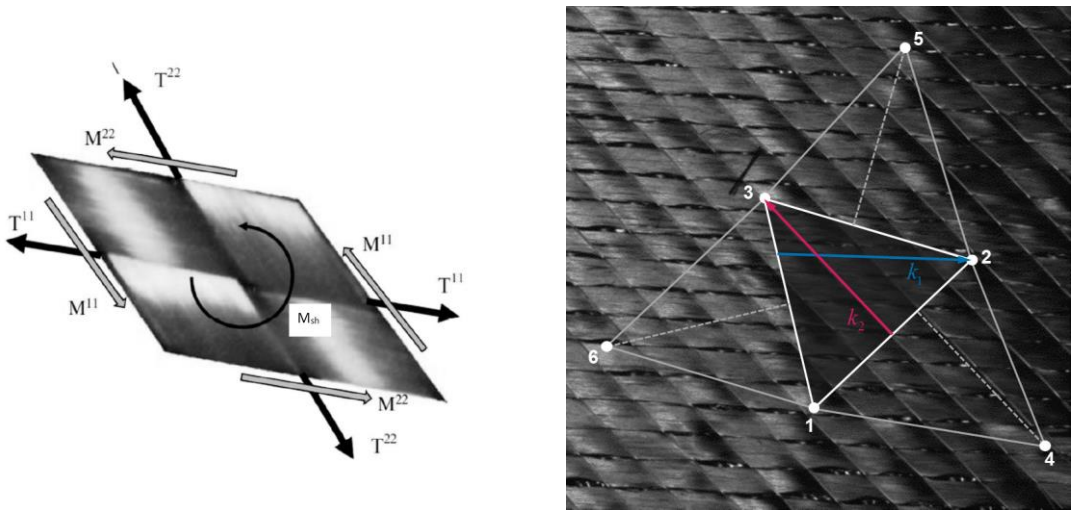

(a) Stress resultants and couple resultants on a unit cell (b) Neighboring nodes used for bending

Figure 7 Stress-resultant shell element for composite forming

3.2. Asymmetrical shear behavior.

As seen before, the asymmetrical behavior of these materials is mainly related to the in-plane shear strains. The expression of the shear moment can be decomposed according to the sign of the shear angle. Polynomial functions can be used to fit this behavior according to:

$$M_{sh}(\gamma) = \begin{cases} \sum_{i=1}^{m} k_i^{+} \gamma^i, & \gamma \geq 0 \\ \sum_{i=1}^{n} k_i^{-} \gamma^i, & \gamma < 0 \end{cases} \tag{35}$$

where k^- and k^+ are the material parameters in the case of negative and positive shear.

The in-plane shear material parameters (Table 1) of the non-orthogonal material (0°/45°), presented in Section 2.5, were identified by using Eq.(35) to fit the experimental shear moment (Fig.6a).

k_1^+	k_2^+	k_3^+	k_4^+	k_5^+	k_1^-	k_2^-	k_3^-	k_4^-	k_5^-	k_6^-	k_7^-	k_8^-	k_9^-
2.0	-42.0	440.3	-2.1e^3	3.7e^3	2.2	40.2	417.5	2.4 e^3	8.3e^3	17.7 e^3	22.8 e^3	16.3 e^3	4.8 e^3

Table 1 In-plane shear parameters of the 0°/45° NCF

3.3. Elementary test

A picture frame test was simulated in the case of a 0/45° fabric. Figure 8a shows the undeformed mesh with the initial warp (green) and weft (red) orientations. Figures 8b and 8c depict the final deformed configurations after negative and positive shears. Finally, Figure 8d presents the comparison between experimental and numerical shear moment curves.

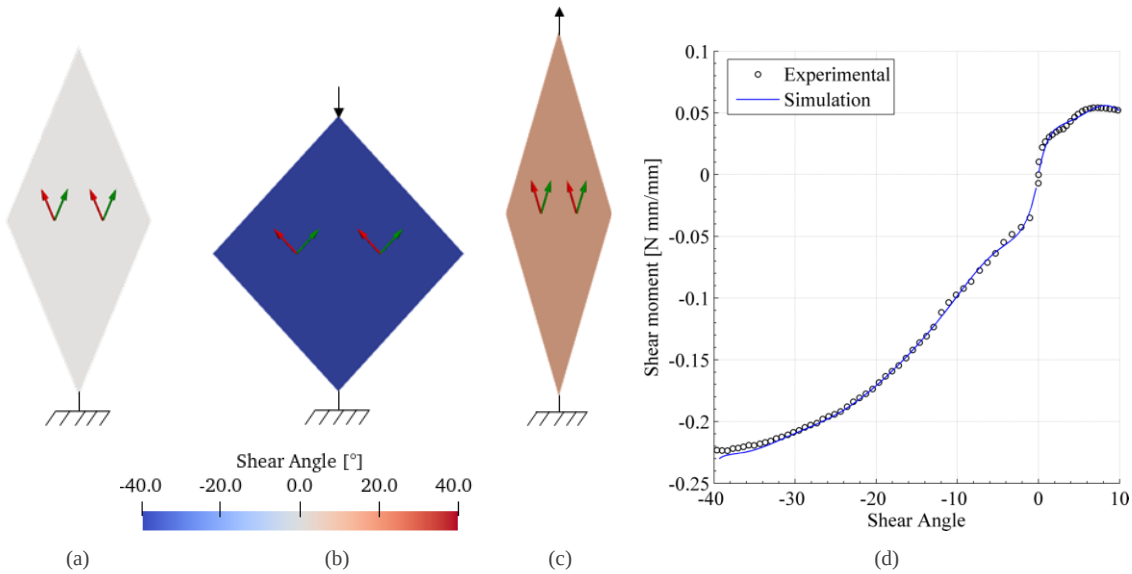

Figure 8 Picture frame simulation. (a) Initial mesh. (b) Deformed mesh after negative shear. (c) Deformed mesh after positive shear. (d) Shear moment versus shear angle

4. Draping simulations

Draping simulations of non-orthogonal fabrics were carried out using the presented stress-resultant shell approach implemented in the research software Plasfib developed at the University of Lyon and by the company Innovamics [63]. The material parameters for tensile and bending behaviors are given in Table 2.

Tension $T^{11}=C_1\varepsilon_{11}$; $T^{22}=C_2\varepsilon_{22}$	$C_1=C_2=1150$ N/yarn
Bending $M^{11}=B_1\chi_{11}$; $M^{22}=B_2\chi_{22}$	$B_1=B_2=0.95$ Nmm
The in-plane shear properties are given in Table 1 for 0/45° NCF and in Table 4 for 0/135° NCF.	
Ply-to-ply and ply-to-tools friction: Coulomb coefficient= 0.2	

Table 2 Mechanical properties of the material

253 *4.1. Hemispherical forming*

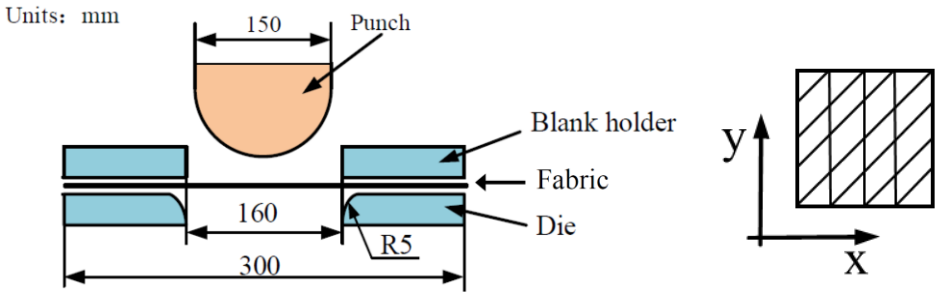

254
255 Figure 9 Diagram of the hemispheric forming device

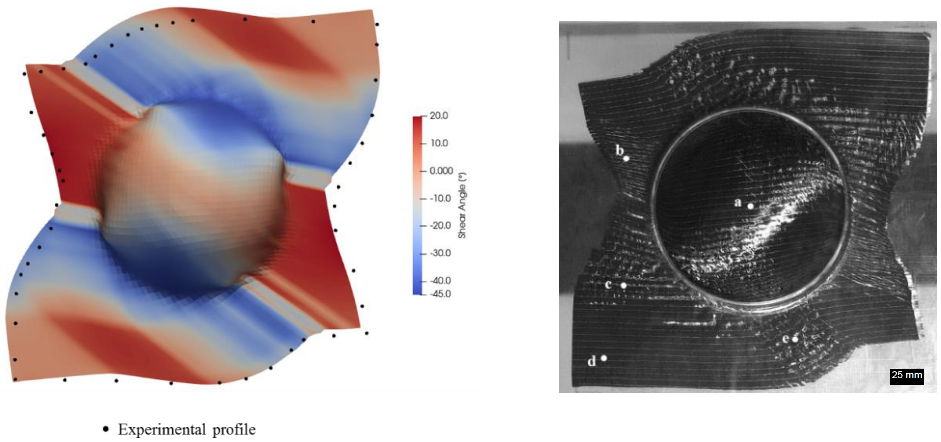

256 Figure 10 Numerical and experimental geometry after hemispherical forming

257 Hemispherical forming of a 0/45° NCF was performed experimentally (Figs. 9 and 10). The simulation was
258 carried out using the in-plane shear behavior determined in section 2. Due to this shear behavior and the
259 orientation of the yarns, the deformed geometry obtained was very specific and significantly different from
260 the classical shape found during the forming of a woven fabric. The boundary of the deformed textile
261 reinforcement was particularly complex. This specific geometry was well achieved by the simulation. The in-
262 plane shear was measured for a set of points marked a to e. The values were compared (Table 3) to the shear
263 angle calculated by the simulation and were found to be in fairly good agreement.

264 This example shows that taking the shear stiffness into account as proposed in section 2 made it possible to
265 describe the specific deformations of non-orthogonal NCFs during draping where plane shear played an
266 important role.

267
268

Point	Experimental Shear Angle	Numerical Shear Angle
a	-2.0	-3.5
b	23	18.2
c	-18	-23

d	0.5	1.18
e	-30	-32

Table 3 Comparison of shear angles measured experimentally and obtained by simulation

4.2. Forming a step profile

The step profile is a very simplified version of an industrial process (Figure 11a). It involves draping an NCF (0°/135°) ply on a step profile. The B edge is clamped and the fabric bends under its own weight. Next, a pressure of 0.05 MPa is applied on the reinforcement for it to come into contact with the step mold (Figure 11b). When the fabric is shaped, a force of 15 N/m is applied on edge A to test the resistance of the preform.

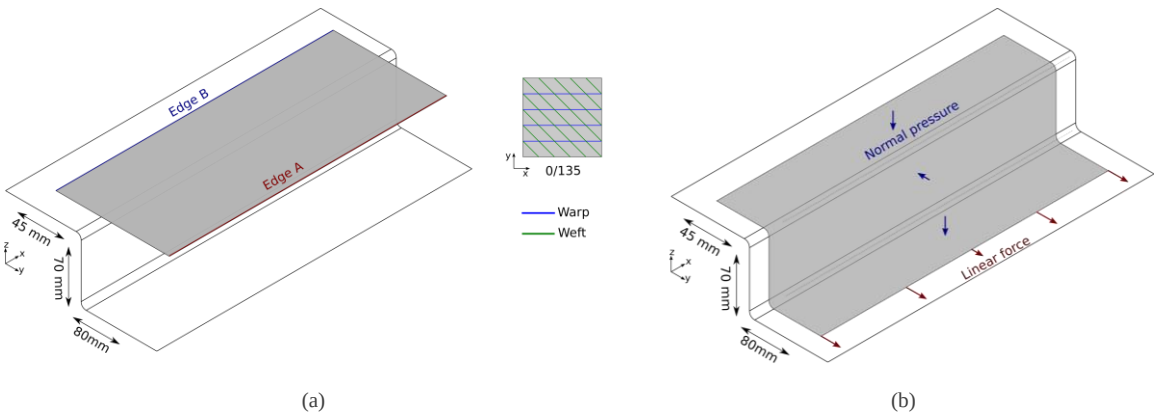

(a) (b)

Figure 11 Step shaped device (a) initial and (b) final configurations.

Figure 12a shows the deformed experimental profile. As expected, the edges remained straight, in particular edge A. However, this simple test made it possible to highlight an important specificity of the behavior of non-orthogonal NCF. By applying a moderate linear force on edge A, while maintaining the normal pressure, a large deformation occurred in a triangular area of the right part of the preform where no fiber under tension opposed this deformation (Figure 12b). The deformed triangular area was of importance for the strength of the composite part obtained from this preform. If the deformation in this triangular area did not occur when no force was applied (Figure 12a), the final composite using this NCF preform would have a significant weakness in this area. Depending on the function of the part, this may be without significance or criticality. In any case, it was important that the numerical simulation be able to highlight the phenomenon.

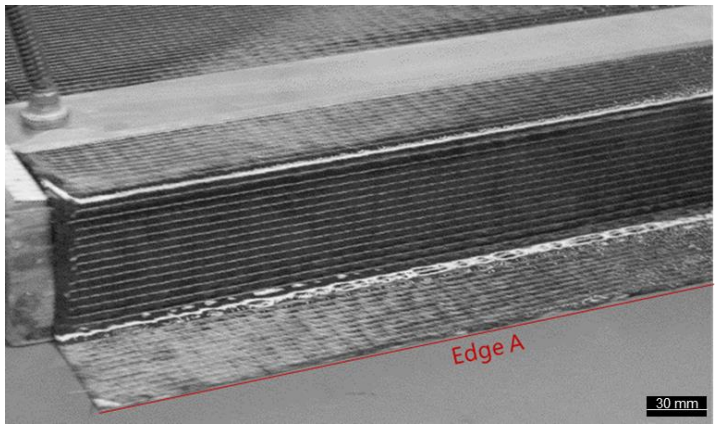

(a)

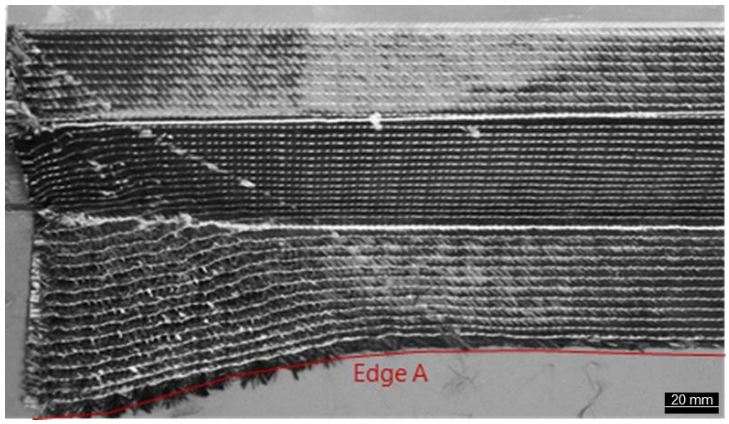

(b)

Figure 12 Experimental step-forming (a) after draping and (b) after applying the linear force.

The following demonstrates that the finite element simulation using the previous model was able to predict this phenomenon. The in-plane shear parameters for the simulation are given in Table 4:

k_1^+	k_2^+	k_3^+	k_4^+	k_5^+	k_1^-	k_2^-	k_3^-	k_4^-	k_5^-	k_6^-	k_7^-	k_8^-	k_9^-
2.2	47,2	497	$2.5e^3$	$4.5e^3$	2.4	-45,2	471	$-2.8\ e^3$	$10e^3$	$-21e^3$	$30\ e^3$	$-22.5\ e^3$	$6.8\ e^3$

Table 4 Material parameters of the 0°/135° NCF

Figure 13a shows the mesh at the initial state, Figure 13b presents the deformed state at the end of the gravity step and Figure 13c depicts the final state at the end of the pressure step. Finally, as can be observed in Figure 13d, a sheared zone was created after applying the linear force. This kinematics was possible due to the orientation of the material and the boundary conditions of the test.

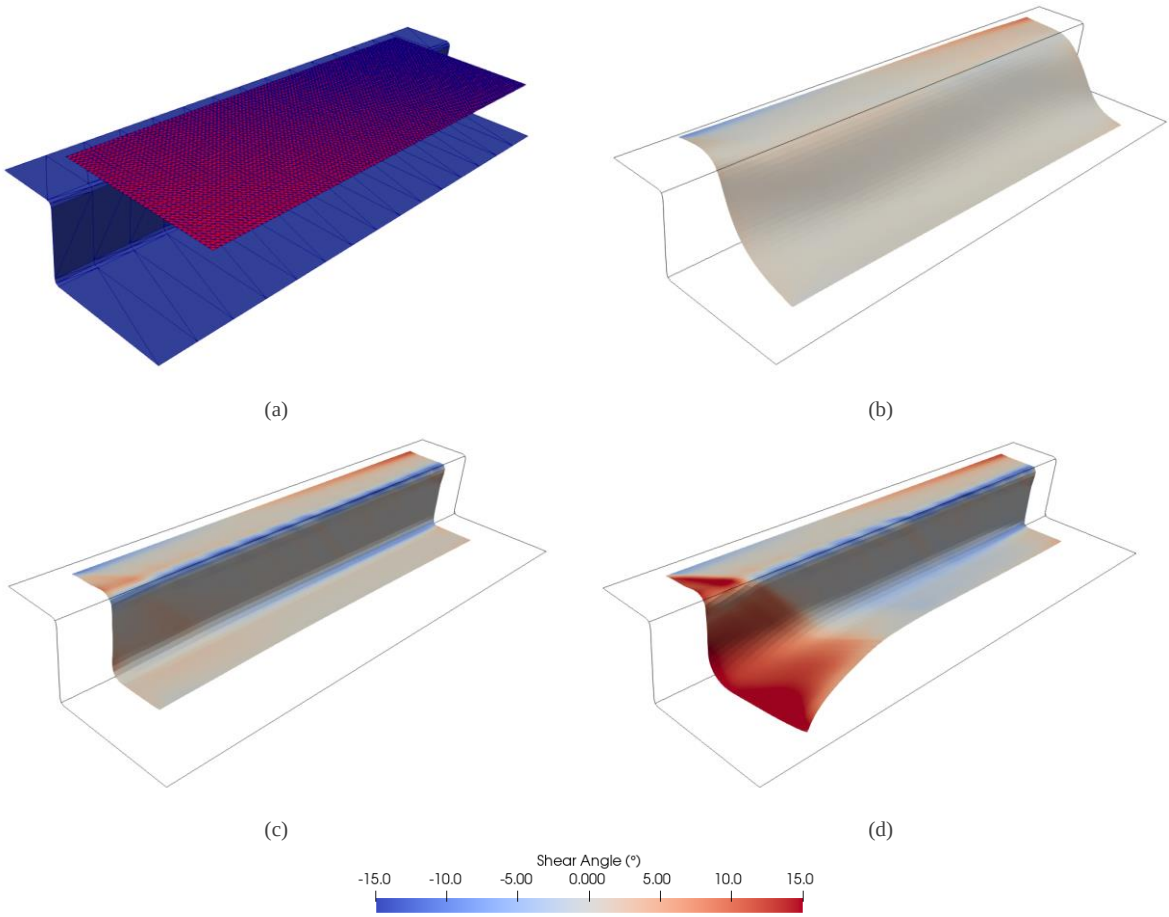

Figure 13 Step-forming simulation steps: (a) initial mesh, (b) gravity, (c) normal pressure and (d) linear tension applied on edge A.

It was observed that the numerical simulation based on the behavior relations presented above was in good agreement with the experiment. As shown in Figure 14, in zone A, there was a "free triangle", i.e., an area in which the yarns were not subjected to any boundary conditions or constraints other than those induced by the stitching. The material could not withstand high tensile stresses in this area, making it weak. On the other hand, in zone B, there was at least one weft yarn clamped at its edge. Therefore, when this composite structure was subjected to tensile stresses in the weft direction, the predominant mode in Zone B was tension, whereas the predominant mode in Zone A was in-plane shear with a very low resistance.

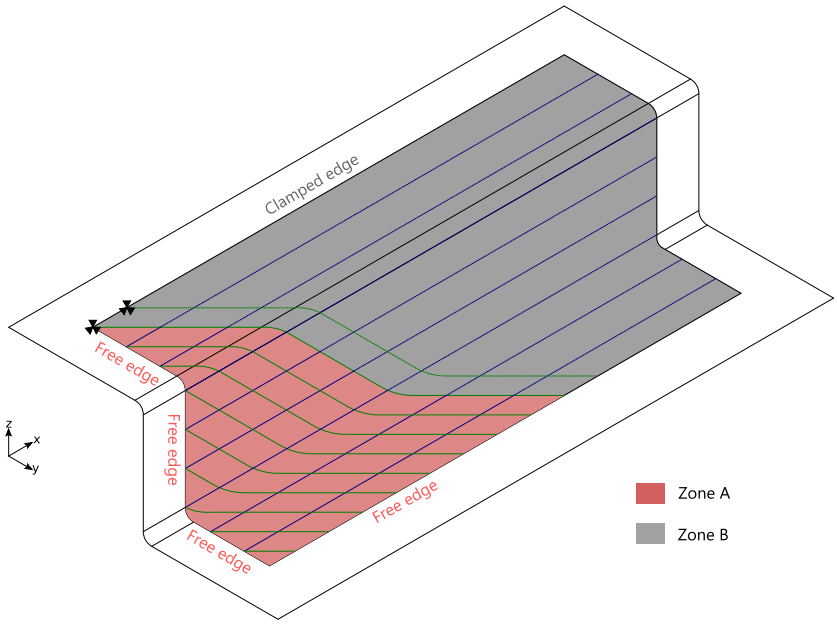

Figure 14 Highlighting the free triangle phenomenon in the step-forming of NCF (0°-135°)

Although these observations were simple, they can have a major impact. First of all, the presence of this easily deformable area might create a weakness in the final composite part. In addition, during the forming of multi-layer reinforcements, the interaction between the different plies generates both compressive and tensile loads through friction, especially when the plies are oriented in different directions [64-66]. These loads can have an important influence on the so-called free zones. Another aspect may concern vacuum forming. When the vacuum bag applies pressure to the reinforcement, the material can get stuck between the mold and the membrane due to clamping caused by normal stress and friction. This induces tension forces in the reinforcement and can change the desired deformation kinematics in these free zones. For a stack with the same orientation (in this case 0°/135°), one must consider that the mechanical properties in this zone will be degraded if the same boundary conditions are maintained.

5. Conclusions

Biaxial NCFs can be manufactured with two sets of fibers that are non-orthogonal, in particular with 0/45° and 0/135° directions. These reinforcements provide different orientations in the laminates and have found widespread use in aeronautics. The mechanical behavior during in-plane shearing, as analyzed by picture frame and bias extension tests, became modified by this non-orthogonal orientation of the two sets of fibers. The equations for this case are given in the present paper and led to different behaviors for positive and negative shear angles. The identified in-plane shear behavior laws were integrated into stress-resultant shell elements so as to simulate the draping process. The results of these simulations were in good agreement with the draping experiments. In order to use non-orthogonal NCF reinforcements, it was important to be able to

carry out draping simulations based on the identification of the reinforcement properties. These simulations provided the internal geometry of the reinforcement after forming, in particular the fiber direction, and the information gained was necessary for the structural calculation of the composite part at the time of its design. Such calculations are essential for the use of materials in aeronautics.

The NCFs used were (0-45°) and (0-135°) since these orientations are currently employed for certain applications. Nevertheless, the identification equations from the picture frame and bias extension tests were valid for any angle between the two yarn directions. It was therefore possible to consider identification tests and draping simulations for materials with any initial angle obtained when manufacturing NCF. An optimization loop, with regard to the process or the structural analysis of the composite part can be considered, with the objective of optimizing the initial angles of the biaxial NCFs used in the manufactured laminate.

Simulations of draping on a step-profile based on these behaviors and a stress-resultant shell approach led to results in good agreement with the experiments. The weakness of the preform in a triangular area was accurately obtained by the simulation.

The next step of this study will consist in experimentally and numerically analyzing the simultaneous forming of reinforcement stacks comprising bi-axial NCFs with orientations (0-45°). The analysis of the consequences of these stacks on the forming process and on the mechanical performance of the manufactured composite parts will determine the relevance of the different stacks.

Acknowledgements

Financial support for this project was provided by the Airbus Manufacturing Engineering Department for Composite Technologies. The authors thank the project manager, the expert and the process engineers for their initiative and for (precious) support.

References

[1] S.G. Hancock, K.D. Potter, The use of kinematic drape modelling to inform the hand lay-up of complex composite components using woven reinforcements, Compos. Part Appl. Sci. Manuf. 37 (2006) 413–422.

[2] A.A. Skordos, C.M. Aceves, M.P.F. Sutcliffe, A simplified rate dependent model of forming and wrinkling of pre-impregnated woven composites, Compos. Part Appl. Sci. Manuf. 38 (2007) 1318–1330.

[3] R.H.W. Ten Thije, R. Akkerman, A multi-layer triangular membrane finite element for the forming simulation of laminated composites, Compos. Part Appl. Sci. Manuf. 40 (2009) 739–753.

[4] C.J. Mitchell, L.M. Dangora, J.A. Sherwood, Investigation into a robust finite element model for composite materials, Finite Elem. Anal. Des. 115 (2016) 1–8.

[5] Boisse P, Hamila N, Madeo A. Modelling the development of defects during composite reinforcements and prepreg forming.Phil. Trans. R. Soc. (2016) A 374: 20150269.

[6] A. Mallach, F. Härtel, F. Heieck, J.-P. Fuhr, P. Middendorf, M. Gude, Experimental comparison of a macroscopic draping simulation for dry non-crimp fabric preforming on a complex geometry by means of optical measurement, J. Compos. Mater. 51 (2017) 2363–2375.

[7] Doerr, D., Joppich, T., Kugele, D., Henning, F., & Kaerger, L. A coupled thermomechanical approach for finite element forming simulation of continuously fiber-reinforced semi-crystalline thermoplastics.

Composites Part A: Applied Science and Manufacturing, 125 (2019), 105508.
[8] Yu, F., Chen, S., Viisainen, J. V., Sutcliffe, M. P. F., Harper, L. T., & Warrior, N. A.. A macroscale finite element approach for simulating the bending behaviour of biaxial fabrics. Composites Science and Technology, 191 (2020) 108078.
[9] Wang, Y., Belnoue, J. P. H., Ivanov, D. S., & Hallett, S. R. Hypo-viscoelastic modelling of in-plane shear in UD thermoset prepregs. Composites Part A: Applied Science and Manufacturing, 146 (2021) 106400.
[10] A.J. Thompson, J.P. Belnoue, S.R. Hallett, Modelling defect formation in textiles during the double diaphragm forming process, Compos. Part B Eng. 202 (2020) 108357.
[11] Ghaedsharaf, M., Brunel, J. E., & Lebel, L. L. Multiscale numerical simulation of the forming process of biaxial braids during thermoplastic braid-trusion: Predicting 3D and internal geometry and fiber orientation distribution. Composites Part A: Applied Science and Manufacturing, 150 (2021), 106637.
[12] P. Hubert, R. Vaziri, A. Poursartip, A two- dimensional flow model for the process simulation of complex shape composite laminates, Int. J. Numer. Methods Eng. 44 (1999) 1–26.
[13] N.C. Correia, F. Robitaille, A.C. Long, C.D. Rudd, P. Šimáček, S.G. Advani, Analysis of the vacuum infusion moulding process: I. Analytical formulation, Compos. Part Appl. Sci. Manuf. 36 (2005) 1645–1656.
[14] O. Guiraud, P.J. Dumont, L. Orgéas, J.-P. Vassal, T.-H. Le, D. Favier, Towards the simulation of mould filling with polymer composites reinforced with mineral fillers and short fibres, Int. J. Mater. Form. 3 (2010) 1313–1326.
[15] C.H. Park, A. Lebel, A. Saouab, J. Breard, W.I. Lee, Modeling and simulation of voids and saturation in liquid composite molding processes, Compos. Part Appl. Sci. Manuf. 42 (2011) 658–668.
[16] X. Zeng, L.P. Brown, A. Endruweit, M. Matveev, A.C. Long, Geometrical modelling of 3D woven reinforcements for polymer composites: Prediction of fabric permeability and composite mechanical properties, Compos. Part Appl. Sci. Manuf. 56 (2014) 150–160.
[17] C. Ghnatios, E. Abisset-Chavanne, C. Binetruy, F. Chinesta, S. Advani, 3D modeling of squeeze flow of multiaxial laminates, J. Non-Newton. Fluid Mech. 234 (2016) 188–200.
[18] S.V. Lomov, I. Verpoest, M. Barburski, J. Laperre, Carbon composites based on multiaxial multiply stitched preforms. Part 2. KES-F characterisation of the deformability of the preforms at low loads, Compos. Part Appl. Sci. Manuf. 34 (2003) 359–370.
[19] D. Mattsson, R. Joffe, J. Varna, Methodology for characterization of internal structure parameters governing performance in NCF composites, Compos. Part B Eng. 38 (2007) 44–57.
[20] V. Koissin, J. Kustermans, S.V. Lomov, I. Verpoest, B. Van Den Broucke, V. Witzel, Structurally stitched NCF preforms: quasi-static response, Compos. Sci. Technol. 69 (2009) 2701–2710.
[21] T.C. Truong, M. Vettori, S. Lomov, I. Verpoest, Carbon composites based on multi-axial multi-ply stitched preforms. Part 4. Mechanical properties of composites and damage observation, Compos. Part Appl. Sci. Manuf. 36 (2005) 1207–1221.
[22] L. Greve, A.K. Pickett, Modelling damage and failure in carbon/epoxy non-crimp fabric composites including effects of fabric pre-shear, Compos. Part Appl. Sci. Manuf. 37 (2006) 1983–2001.
[23] K. Vallons, M. Zong, S.V. Lomov, I. Verpoest, Carbon composites based on multi-axial multi-ply stitched preforms–Part 6. Fatigue behaviour at low loads: Stiffness degradation and damage development, Compos. Part Appl. Sci. Manuf. 38 (2007) 1633–1645.
[24] H. Kong, A.P. Mouritz, R. Paton, Tensile extension properties and deformation mechanisms of multiaxial non-crimp fabrics, Compos. Struct. 66 (2004) 249–259.
[25] S.V. Lomov, M. Barburski, T. Stoilova, I. Verpoest, R. Akkerman, R. Loendersloot, R. Ten Thije, Carbon composites based on multiaxial multiply stitched preforms. Part 3: Biaxial tension, picture frame and compression tests of the preforms, Compos. Part Appl. Sci. Manuf. 36 (2005) 1188–1206.
[26] F.J. Schirmaier, K.A. Weidenmann, L. Kärger, F. Henning, Characterisation of the draping behaviour of unidirectional non-crimp fabrics (UD-NCF), Compos. Part Appl. Sci. Manuf. 80 (2016) 28–38.
[27] W.-R. Yu, P. Harrison, A. Long, Finite element forming simulation for non-crimp fabrics using a non-orthogonal constitutive equation, Compos. Part Appl. Sci. Manuf. 36 (2005) 1079–1093.
[28] F.J. Schirmaier, D. Dörr, F. Henning, L. Kärger, A macroscopic approach to simulate the forming behaviour of stitched unidirectional non-crimp fabrics (UD-NCF), Compos. Part Appl. Sci. Manuf. 102

(2017) 322–335.
[29] S. Bel, P. Boisse, F. Dumont, Analyses of the deformation mechanisms of non-crimp fabric composite reinforcements during preforming, Appl. Compos. Mater. 19 (2012) 513–528.
[30] S. Bel, N. Hamila, P. Boisse, F. Dumont, Finite element model for NCF composite reinforcement preforming: Importance of inter-ply sliding, Compos. Part Appl. Sci. Manuf. 43 (2012) 2269–2277.
[31] G. Lebrun, M.N. Bureau, J. Denault, Evaluation of bias-extension and picture-frame test methods for the measurement of intraply shear properties of PP/glass commingled fabrics, Compos. Struct. 61 (2003) 341–352.
[32] P. Harrison, M.J. Clifford, A.C. Long, Shear characterisation of viscous woven textile composites : a comparison between picture frame and bias extension experiments, Compos Sci Technol. 64 (2004) 1453–1465.
[33] S.V. Lomov, A. Willems, I. Verpoest, Y. Zhu, M. Barburski, Tz. Stoilova, Picture Frame Test of Woven Composite Reinforcements with a Full-Field Strain Registration, Text. Res. J. 76 (2006) 243–252. https://doi.org/10.1177/0040517506061032.
[34] B. Zhu, T.X. Yu, X.M. Tao, Large deformation and slippage mechanism of plain woven composite in bias extension, Compos. Part Appl. Sci. Manuf. 38 (2007) 1821–1828.
[35] J. Cao, R. Akkerman, P. Boisse, J. Chen, H.S. Cheng, et al. Characterization of mechanical behavior of woven fabrics: Experimental methods and benchmark results, Compos. Part Appl. Sci. Manuf. 39 (2008) 1037–1053.
[36] P. Boisse, N. Hamila, E. Guzman-Maldonado, A. Madeo, G. Hivet, F. dell'Isola, The bias-extension test for the analysis of in-plane shear properties of textile composite reinforcements and prepregs: a review, Int. J. Mater. Form. 10 (2017) 473–492.
[37] Pourtier, J., Duchamp, B., Kowalski, M., Wang, P., Legrand, X., & Soulat, D. Two-way approach for deformation analysis of non-crimp fabrics in uniaxial bias extension tests based on pure and simple shear assumption. International Journal of Material Forming, 12(6) (2019) 995-1008.
[38] Wang, Y., Chea, M. K., Belnoue, J. P. H., Kratz, J., Ivanov, D. S., & Hallett, S. R. Experimental characterisation of the in-plane shear behaviour of UD thermoset prepregs under processing conditions. Composites Part A: Applied Science and Manufacturing, 133 (2020) 105865.
[39] Y. Denis, E. Guzman-Maldonado, N. Hamila, J. Colmars, F. Morestin, A dissipative constitutive model for woven composite fabric under large strain, Compos. Part Appl. Sci. Manuf. 105 (2018) 165–179.
[40] T. Gereke, O. Dobrich, M. Hubner, C. Cherif, Experimental and computational composite textile reinforcement forming: A review, Compos. Part Appl. Sci. Manuf. 46 (2013) 1–10.
[41] Bussetta P, Correia N. Numerical forming of continuous fibre reinforced composite material: a review. Compos A Appl Sci Manuf (2018);113:12–31.
[42] G. Creech, A.K. Pickett, Meso-modelling of Non-Crimp Fabric composites for coupled drape and failure analysis, J. Mater. Sci. 41 (2006) 6725–6736.
[43] S. Gatouillat, A. Bareggi, E. Vidal-Sallé, P. Boisse, Meso modelling for composite preform shaping - Simulation of the loss of cohesion of the woven fibre network, Compos. Part Appl. Sci. Manuf. 54 (2013) 135–144.
[44] A. Iwata, T. Inoue, N. Naouar, P. Boisse, S.V. Lomov, Coupled meso-macro simulation of woven fabric local deformation during draping., Compos. Part Appl. Sci. Manuf. 118 (2019) 267–280.
[45] W.R. Yu, F. Pourboghrat, K. Chung, M. Zampaloni, T.J. Kang, Non-orthogonal constitutive equation for woven fabric reinforced thermoplastic composites, Compos. Part Appl. Sci. Manuf. 33 (2002) 1095–1105.
[46] X.Q. Peng, J. Cao, A continuum mechanics-based non-orthogonal constitutive model for woven composite fabrics, Compos. Part Appl. Sci. Manuf. (2005).
[47] M.A. Khan, T. Mabrouki, E. Vidal-Sallé, P. Boisse, Numerical and experimental analyses of woven composite reinforcement forming using a hypoelastic behaviour. Application to the double dome benchmark, J. Mater. Process. Technol. 210 (2010) 378–388.
[48] A. Milani, J. Nemes, An intelligent inverse method for characterization of textile reinforced thermoplastic composites using a hyperelastic constitutive model, Compos. Sci. Technol. 64 (2004) 1565–1576.
[49] Peng XQ, Guo ZY, Du T, et al. A simple anisotropic hyperelastic constitutive model for textile fabrics

with application to forming simulation. Compos B Eng;52 (2013) 275–81.
[50] E. Guzman-Maldonado, N. Hamila, N. Naouar, G. Moulin, P. Boisse, Simulation of thermoplastic prepreg thermoforming based on a visco-hyperelastic model and a thermal homogenization, Mater. Des. 93 (2016) 431–442.
[51] E. Guzman-Maldonado, N. Hamila, P. Boisse, J. Bikard, Thermomechanical analysis, modelling and simulation of the forming of pre-impregnated thermoplastics composites, Compos. Part Appl. Sci. Manuf. 78 (2015) 211–222.
[52] Y. Gong, X. Peng, Y. Yao, Z. Guo, An anisotropic hyperelastic constitutive model for thermoplastic woven composite prepregs, Compos. Sci. Technol. 128 (2016) 17–24.
[53] X. Su, Y. Wang, X. Peng, An anisotropic visco-hyperelastic model for thermally-actuated shape memory polymer-based woven fabric-reinforced composites, Int. J. Plast. 129 (2020) 102697.
[54] Peng XQ, Rehman ZU. Textile composite double dome stamping simulation using a non-orthogonal constitutive model. Compos Sci Technol; 71(8) (2011)1075–81.
[55] J.C. Simo, D.D. Fox, On a stress resultant geometrically exact shell model. Part I: Formulation and optimal parametrization, Comput. Methods Appl. Mech. Eng. 72 (1989) 267–304.
[56] A. Ibrahimbegović, Stress resultant geometrically nonlinear shell theory with drilling rotations—Part I. A consistent formulation, Comput. Methods Appl. Mech. Eng. 118 (1994) 265–284.
[57] N. Hamila, P. Boisse, F. Sabourin, M. Brunet, A semi-discrete shell finite element for textile composite reinforcement forming simulation, Int. J. Numer. Methods Eng. 79 (2009) 1443–1466.
[58] T. Belytschko, An overview of semidiscretization and time integration procedures, Comput. Methods Transient Anal. 84-29160 12-64 Amst. N.-Holl. 1983. (1983) 1–65.
[59] T. Belytschko, J.I. Lin, T. Chen-Shyh, Explicit algorithms for the nonlinear dynamics of shells, Comput. Methods Appl. Mech. Eng. 42 (1984) 225–251.
[60] E. Onate, F. Zarate, Rotation-free triangular plate and shell elements, Int. J. Numer. Methods Eng. 47 (2000) 557–603.
[61] F. Sabourin, M. Brunet, Detailed formulation of the rotation-free triangular element S3 for general purpose shell analysis, Eng. Comput. 23 (2006) 469–502.
[62] Wang, X., & Zhou, G. (2021). A rotation-free quadrature element formulation for free vibration analysis of thin sectorial plates with arbitrary boundary supports. Computers & Mathematics with Applications, 99, 84-98.
[63] Software PLASFIB, Paris, Inter Deposit Certification, agence pour la protection des programmes. 2011 and 2015.
[64] E. Guzman-Maldonado, P. Wang, N. Hamila, P. Boisse, Experimental and numerical analysis of wrinkling during forming of multi-layered textile composites, Compos. Struct. 208 (2019) 213–223.
[65] Yu, F., Chen, S., Harper, L. T., & Warrior, N. A. Double diaphragm forming simulation using a global-to-local modelling strategy for detailed defect detection in large structures. Composites Part A: Applied Science and Manufacturing, 147 (2021) 106457.
[66] Yu, F., Chen, S., Harper, L. T., & Warrior, N. A. Investigation into the effects of inter-ply sliding during double diaphragm forming for multi-layered biaxial non-crimp fabrics. Composites Part A: Applied Science and Manufacturing, 150 (2021) 106611.

Non-orthogonal non-crimp fabrics (NCF) | **Testing** | **Modelling**

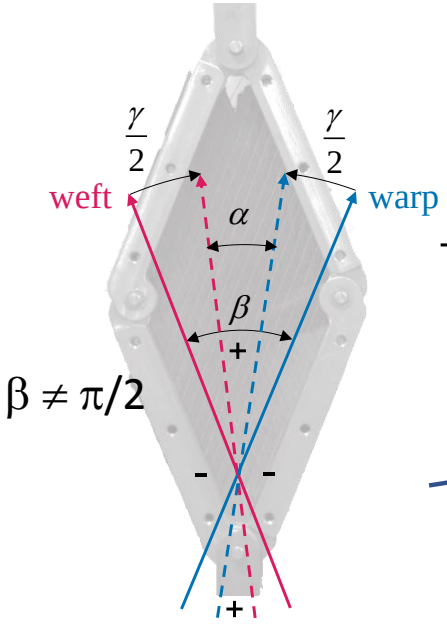

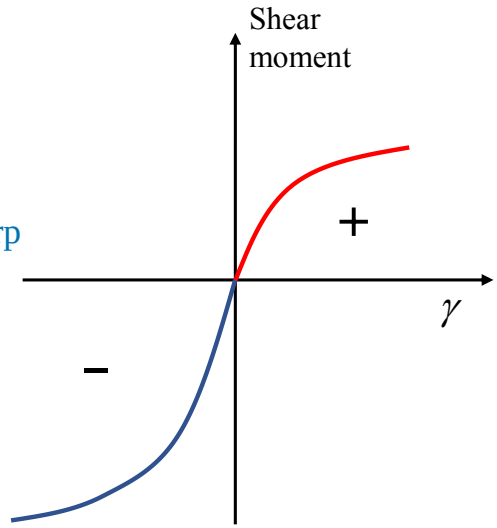

$\gamma(t) = \beta - \alpha(t)$

Shear angle

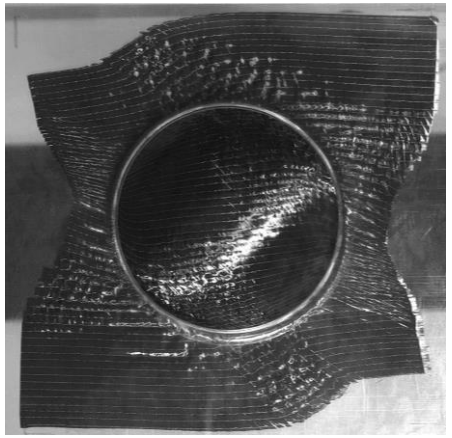

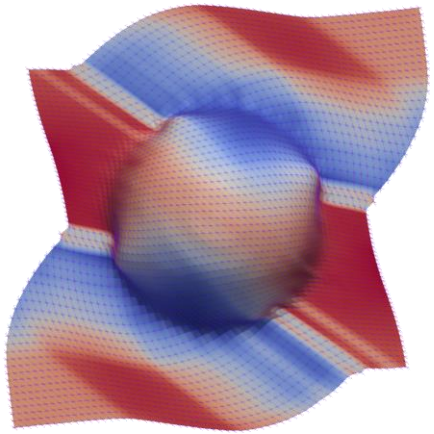

Asymmetrical behavior